Virologica Sinica 40 (2025) 225–235

Contents lists available at ScienceDirect

Virologica Sinica

journal homepage: www.keaipublishing.com/en/journals/virologica-sinica
www.virosin.org

Research Article

The SARS-CoV-2 NSP4 T492I mutation promotes double-membrane vesicle formation to facilitate transmission

Pei Wang [a,b], Buyun Tian [a,b], Ke Xiao [c], Wei Ji [c], Zonghong Li [a,b,*]

[a] The First Affiliated Hospital of Guangzhou Medical University, Guangzhou National Laboratory Clinical Base, Guangzhou Medical University, Guangzhou, 510120, China
[b] Guangzhou National Laboratory, Guangzhou, 510005, China
[c] National Laboratory of Biomacromolecules, CAS Center for Excellence in Biomacromolecules, Institute of Biophysics, Chinese Academy of Sciences, Beijing, 100101, China

ARTICLE INFO

Keywords:
SARS-CoV-2
Virus transmission
NSP4 T492I mutation
DMV
Homodimerization
ER membrane curvature

ABSTRACT

The evolution of severe acute respiratory syndrome coronavirus 2 (SARS-CoV-2) has resulted in mutations not only in the spike protein, aiding immune evasion, but also in the NSP3/4/6 proteins, crucial for regulating double-membrane vesicle (DMV) formation. However, the functional consequences of these NSP3/4/6 mutations remain poorly understood. In this study, a systematic analysis was conducted to investigate the evolutionary patterns of NSP3/4/6 mutations and their impact on DMV formation. The findings revealed that the NSP4 T492I mutation, a prevalent mutation found in all Delta and Omicron sub-lineages, notably enhances DMV formation. Mechanistically, the NSP4 T492I mutation enhances its homodimerization, leading to an increase in the size of puncta induced by NSP3/4, and also augments endoplasmic reticulum (ER) membrane curvature, resulting in a higher DMV density per fluorescent puncta. This study underscores the significance of the NSP4 T492I mutation in modulating DMV formation, with potential implications for the transmission dynamics of SARS-CoV-2. It contributes valuable insights into how these mutations impact viral replication and pathogenesis.

INTRODUCTION

Since the beginning of the COVID-19 pandemic, severe acute respiratory syndrome coronavirus 2 (SARS-CoV-2) continues to evolve, and multiple variants of concern (VOCs) and variants of interest (VOIs) have been designated by World Health Organization (WHO) based on their assessed potential for expansion and replacement of prior variants, including Alpha (B.1.1.7), Beta (B.1.351), Gamma (P.1), Delta (B.1.617.2 and AY sub-lineages) and Omicron (BA, XBB, EG and JN sub-lineages) (WHO, 2024). Omicron was first documented in South Africa, Botswana and in a traveler from South Africa in Hong Kong in November 2021 (Gu et al., 2022). It quickly swept through the world, displacing the previously dominant Delta variant within weeks and accounting for most new SARS-CoV-2 infections by January 2022. As of June 2024, SARS-CoV-2 has evolved into EG, XBB and JN sub-lineages. Genomic variations and the emergence of adaptive mutations have facilitated the rapid spread of the VOCs and VOIs. Functional analyses of these significant mutations not only offer insights into the emergence of VOCs and the evolutionary trajectory of SARS-CoV-2 but also enhance our understanding of the molecular and cellular mechanisms of SARS-CoV-2 infection.

The spike protein of SARS-CoV-2 has undergone significant mutations that enhance and stabilize its binding to the receptor ACE2, promoting viral entry, and allowing the virus to escape antibody recognition (Harvey et al., 2021; Souza et al., 2022). The initial observation of this phenomenon was with the D614G mutation (Hou et al., 2020; Yurkovetskiy et al., 2020). Subsequent VOCs such as Alpha, Delta, and Omicron have displayed mutations that further enhance binding affinity, with the N501Y mutation in the receptor binding domain (RBD) being a notable example (Xie et al., 2021). In descendants of the BA.4 and BA.5 sub-lineages of Omicron, additional mutations in the RBD, including L452R and F486V, have been identified (Deng et al., 2021; Tchesnokova et al., 2021; Cao et al., 2022). These mutations have been shown to

* Corresponding author.
E-mail address: li_zonghong@gzlab.ac.cn (Z. Li).

https://doi.org/10.1016/j.virs.2025.03.010
Received 24 December 2024; Accepted 24 March 2025
Available online 28 March 2025

contribute significantly to the ability of these variants to evade immune responses (Deng et al., 2021; Tchesnokova et al., 2021; Cao et al., 2022). Furthermore, mutations in the nucleocapsid protein, such as R203K and G204R, have been associated with increased viral replication and transmissibility (Wu et al., 2021). Mutations in genes like ORF9b and ORF6 can lead to evasion of the innate immune response and enhance viral transmission (Thorne et al., 2022; Kehrer et al., 2023). These mutations collectively contribute to the evolving landscape of SARS-CoV-2 variants and their ability to evade host immunity and facilitate viral spread.

Except for the viral structural proteins and accessary proteins, mutations in non-structural proteins (NSPs), such as NSP3 (K38R, S1265Δ, L1266I and A1892T), NSP4 (T492I), and NSP6 (LSG105, 106, 107Δ and I189V), have been observed in the Omicron BA.1 variant of SARS-CoV-2 (Chen et al., 2023). Studies have revealed that NSP3, NSP4, and NSP6 play vital roles in the regulation of double-membrane vesicles (DMVs) formation, which serve as the replication sites for coronaviruses (Angelini et al., 2013). DMVs are densely packed with dsRNA, believed to function as the replication intermediate during viral RNA synthesis (Knoops et al., 2008; Klein et al., 2020). Recent research has identified a molecular pore spanning the DMV, suggested to serve as a viral RNA export channel in cells infected by coronaviruses (Wolff et al., 2020). Ectopic expression of NSP3 and NSP4 alone has been shown to induce DMV-like structures resembling those observed in infected cells (Tabata et al., 2021; Zimmermann et al., 2023; Yang et al., 2025). NSP6, on the other hand, acts as an organizer of DMV clusters and facilitates contact with lipid droplets (Ricciardi et al., 2022). Specific mutations in these NSPs, such as the T492I mutation in NSP4, have been found to enhance SARS-CoV-2 infectivity by increasing the cleavage efficiency of the viral main protease NSP5 (Lin et al., 2023). The NSP6 mutations have been linked to the attenuated phenotype of the Omicron variant (Chen et al., 2023). However, the precise effects of these mutations on DMV formation remain largely unknown and require further investigation. Furthermore, the evolution of these mutations and their correlation with DMVs should be further explored.

In this study, we systematically analyzed the evolutionary patterns of NSP3/4/6 mutations and their impact on DMV formation. The NSP4 T492I mutation, a prevalent mutation found in all Delta and Omicron sub-lineages, significantly enhances DMV formation, while the NSP3 and NSP6 mutations do not have the same effect. Mechanistically, the NSP4 T492I mutation promotes its homodimerization, leading to the enlargement of puncta induced by NSP3/4. In addition, NSP4 T492I mutation increases ER membrane curvature, resulting in an increase in DMV density per fluorescent puncta. Overall, our findings underscore the significance of the NSP4 T492I mutation in modulating DMV formation and in the evolutionary dynamics of SARS-CoV-2.

RESULTS

The SARS-CoV-2 NSP4 T492I mutation promotes DMV formation

To systematically analysis the effect of NSP3 (K38R, S1265Δ, L1266I and A1892T), NSP4 (T492I), and NSP6 (LSG105, 106, 107Δ and I189V) mutations on the DMV formation, co-expressing of the NSP3 (WT)/NSP4 (WT)/NSP6 (WT), NSP3 (WT)/NSP4 (WT)/NSP6 (all mutations), NSP3 (all mutations)/NSP4 (WT)/NSP6 (WT), NSP3 (all mutations)/NSP4 (T492I)/NSP6 (all mutations), NSP3 (all mutations)/NSP4 (T492I)/NSP6 (WT), and NSP3 (WT)/NSP4 (T492I)/NSP6 (WT) cells were subjected to transmission electron microscope (TEM) analysis (Fig. 1A). Quantitative analysis of TEM results revealed two distinct patterns: NSP3 (WT)/NSP4 (WT)/NSP6 (WT), NSP3 (all mutations)/NSP4 (WT)/NSP6 (WT) and NSP3 (WT)/NSP4 (WT)/NSP6 (all mutations) displayed low DMV numbers, while NSP3 (all mutations)/NSP4 (T492I)/NSP6 (all mutations), NSP3 (WT)/NSP4 (T492I)/NSP6 (WT) and NSP3 (all mutations)/NSP4 (T492I)/NSP6 (WT) exhibited high DMV numbers and decreased DMV sizes (Fig. 1B–D). Immunoblotting (IB) results showed that these mutations have no effect on the protein expression levels (Fig. 1E). These results suggested that only the NSP4 T492I mutation promotes DMV formation, with NSP3 and NSP6 mutations showing no significantly impact on DMV formation. Furthermore, co-expressing of the NSP3 (WT)/NSP4 (WT) and NSP3 (WT)/NSP4 (T492I), where NSP3 and NSP4 were linked with T2A, consistently showed higher DMV numbers in cells expressing NSP3 (WT)/NSP4 (T492I) compared to NSP3 (WT)/NSP4 (WT) cells (Fig. 1F and G). These results indicate the NSP4 T492I mutation promotes DMV formation.

NSP4 T492I mutation dominates from Delta to all Omicron sub-lineages

These mutations were observed in the Omicron BA.1 variant of SARS-CoV-2, which was first documented in South Africa in November 2021 (Chen et al., 2023). As of June 2024, SARS-CoV-2 has evolved into EG, XBB and JN sub-lineages. Analysis of genomic sequences from various VOCs provided by Global Initiative on Sharing Avian Influenza Data (GISAID) revealed that only NSP4 T492I mutation was consistently present across all Omicron sub-lineages, from the Delta variant onwards (Fig. 2A and B). In contrast, NSP3 (K38R, S1265Δ and L1266I) and NSP6 (LSG105Δ and I189V) mutations were unique to the Omicron BA.1 variant and not observed in the EG, XBB, and JN sub-lineages (Fig. 2B). NSP3 (A1892T) mutation was primarily found in the Omicron BA.1 and JN.1 sub-lineages. Additionally, NSP6 (S106Δ and G107Δ) mutations emerged independently in the Alpha, Beta, Gamma and Omicron variants but were absent in the Delta variant (Fig. 2B). Considering the influence of NSP4 (T492I) on DMV formation, these results underscore the critical role of the NSP4 T492I mutation in the fitness and transmission dynamics of SARS-CoV-2.

NSP4 T492I mutation does not affect its stability and its interaction with NSP3

To explore the mechanism underlying the NSP4 T492I mutation promoting DMV formation, we first examined the impact of this mutation on NSP4 expression and stability. Protein expression and decay analyses revealed comparable levels between NSP4 (WT) and NSP4 (T492I), suggesting that the T492I mutation did not alter NSP4 expression or stability (Fig. 3A and B). Given the crucial role of the interaction between NSP3 and NSP4 in DMV formation, we further investigated whether the T492I mutation affected this interaction. By co-expressing NSP3 with either NSP4 (WT) or NSP4 (T492I), co-immunoprecipitation (Co-IP) results demonstrated that similar amounts of NSP4 (WT) and NSP4 (T492I), pulled down by the FLAG antibody, could precipitate equivalent amounts of NSP3 (Fig. 3C and D). Conversely, the same amount of NSP3 could precipitate comparable levels of both NSP4 (WT) and NSP4 (T492I) (Fig. 3E and F). These findings indicate that the NSP4 T492I mutation does not impair its interaction with NSP3.

Then we explored whether host factors are involved in the NSP4 T492I mutation induced DMV formation increase. Immunoprecipitated proteins pulled down by NSP4 (WT) and NSP4 (T492I), as well as NSP3-T2A-NSP4 (WT) and NSP3-T2A-NSP4 (T492I), were identified using mass spectrometry (MS). The NSP3-T2A-NSP4 construct was used to rule out the possibility that the immunoprecipitated proteins interacted with NSP4 only in the ER and were not involved in DMV formation. Quantitative analyses of the interaction proteins between the NSP4 (WT) and NSP4 (T492I) revealed that the mutation affected the expression level of a very minute number of proteins in both NSP4 and NSP3-T2A-NSP4 groups, with no significant change of previously known host factors involved in DMV formation (Supplementary Fig. S1A–C). The correlation plot analysis of proteins enriched in NSP4 T492I mutation compared to WT in both NSP4 and NSP3-T2A-NSP4 groups identified limited proteins as significant changes (Supplementary Fig. S1A). Given that DMVs originate from the host ER and known DMV regulators are ER membrane proteins that co-localize with DMVs, the study aimed to determine

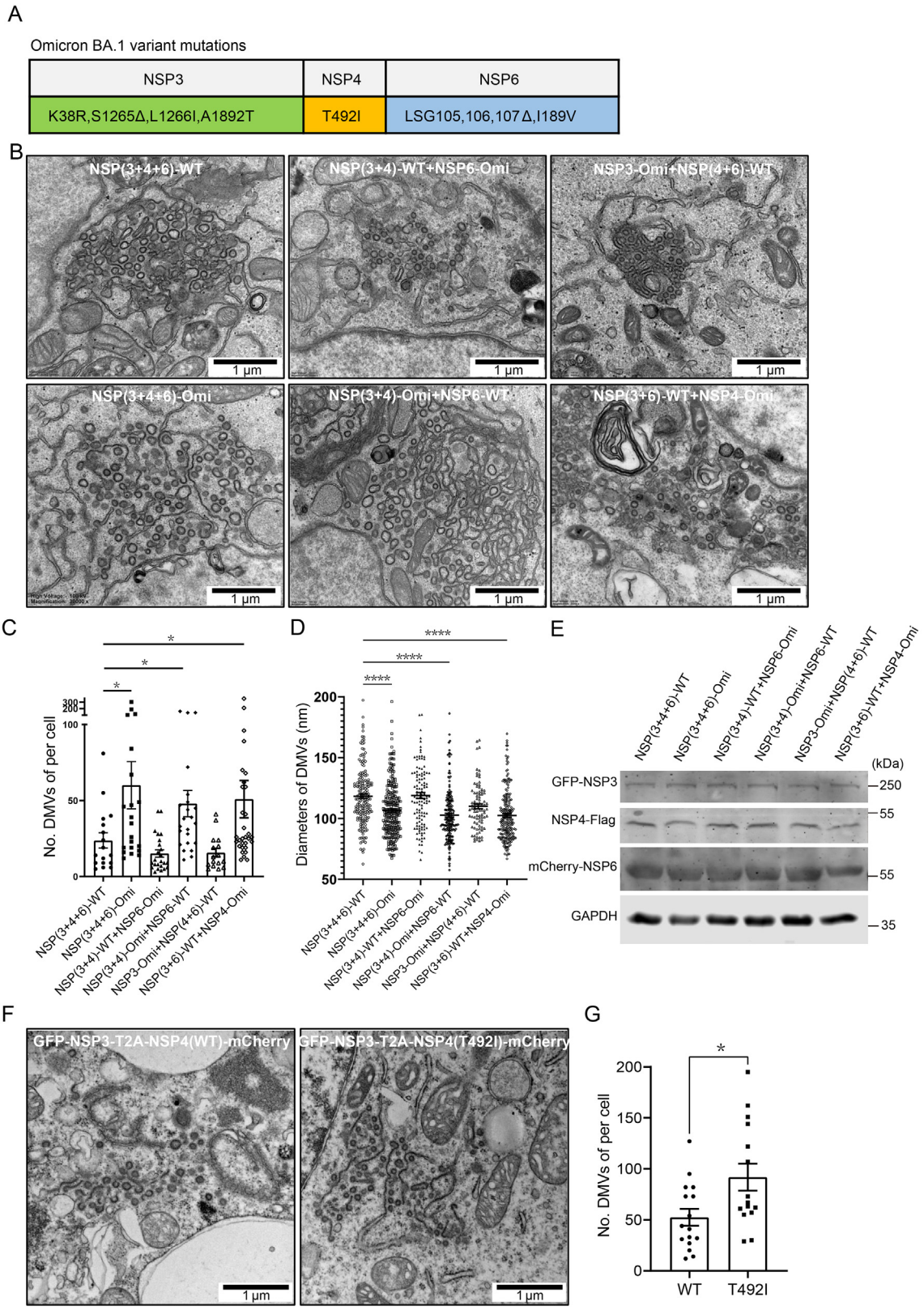

Fig. 1. The SARS-CoV-2 NSP4 T492I mutation promotes DMV formation. **A** Schematic diagram of mutation sites of NSP3, NSP4 and NSP6 in Omicron BA.1 variant. **B** Conventional TEM images of DMV in HeLa cells induced by NSP3/4/6 with different mutations. **C** Statistical analysis of DMV numbers per cell. Mean ± SEM, N = 3, n = 16 (in all figure legends, N indicates the number of independent experiments and n indicates the number of total measurements or observations). **D** Statistical analysis of DMV diameters in different mutation samples. Mean ± SEM, N = 3, n = 8. **E** Immunoblotting of NSPs protein expression level in different mutation. **F** Conventional TEM images of DMV in HEK293T cells induced by NSP3/4. **G** Statistical analysis of DMV numbers per cell. N = 3, n = 15. All data are shown as mean ± SEM, using unpaired two-tailed *t*-test, $^*P < 0.05$, significant.

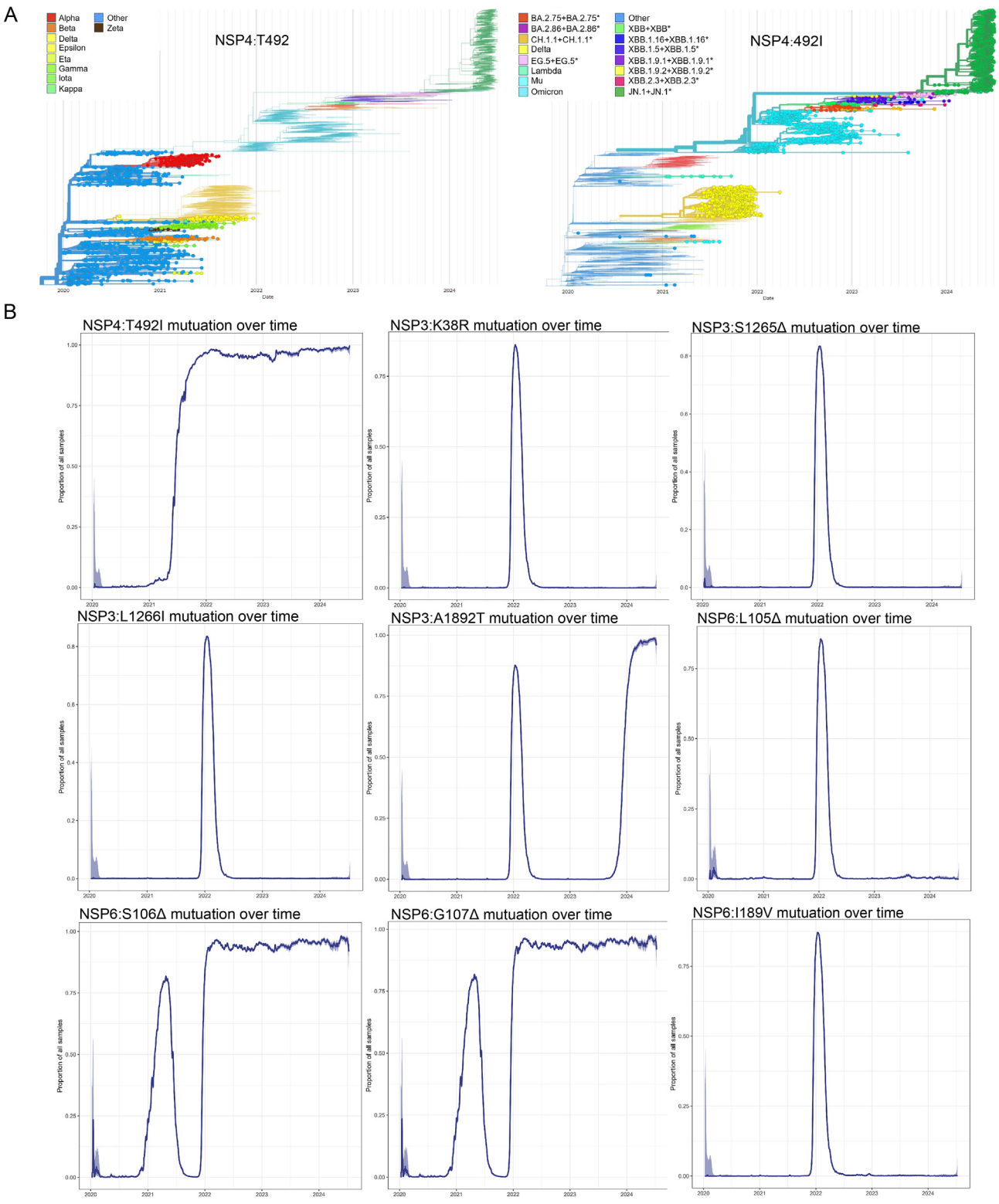

Fig. 2. Phylogeny of NSP3, NSP4, NSP6 mutations in 3986 SARS-CoV-2 genomes from 2020 to 2024. **A** A phylogenetic tree of SARS-CoV-2 strains showing the T492I mutation associated VOCs, marked with circle (generated by the GISAID database). **B** The ratio of NSP3, NSP4, NSP6 mutations from 2020 to 2024 (generated by the covSPECTRUM).

whether these membrane proteins could be recruited to DMVs induced by NSP3/4. However, upon co-expressing these membrane proteins with NSP3/4, no significant co-localization with the NSP3/4^{+} puncta were observed (Supplementary Fig. S1D), suggesting that these specific host factors may not play a significant role in DMV formation in this context.

NSP4 T492I mutation increases its homodimerization and the size of puncta induced by NSP3/4

Previous study showed that the NSP4 can form homodimers (Hagemeijer et al., 2011), promoting us to hypothesize that whether

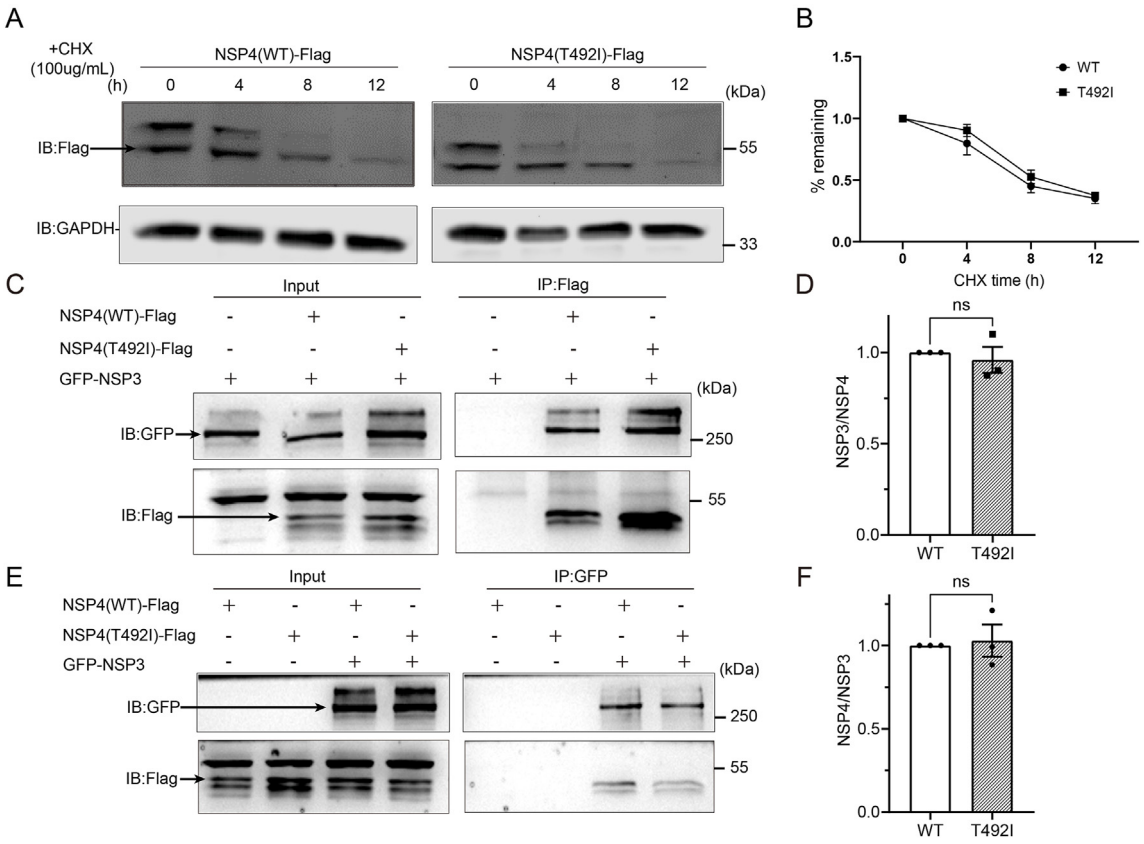

Fig. 3. NSP4 T492I mutation does not affect its stability and its interaction with NSP3. **A** To assess whether the T492I mutation affected the stability of NSP4, HEK293T cells transfected with NSP4(WT)-FLAG or NSP4(T492I)-FLAG were treated with cycloheximide (CHX) to block nascent protein synthesis for the time points 0, 4, 8, 12 h, and the stability of NSP4 protein was assessed by immunoblotting. **B** The fold change in NSP4 expression was calculated by normalization to GAPDH expression. N = 3. Data are presented as mean ± SEM, using repeat measures two-way ANOVA. **C–F** Co-IP analysis of the effect of T492I mutation on the interaction between NSP3 and NSP4. HEK293T cells co-expressing GFP-NSP3 and NSP4-FLAG (WT or T492I mutation) were lysed, and immunoprecipitates pulled down by FLAG antibody were analyzed by immunoblotting with the indicated antibodies (**C**). The fold change in immunoprecipitated GFP-NSP3 was calculated by normalization to immunoprecipitated NSP4-FLAG. N = 3 (**D**). HEK293T cells co-expressing GFP-NSP3 and NSP4-FLAG (WT or T492I mutation) were lysed, and immunoprecipitates pulled down by GFP antibody were analyzed by immunoblotting with the indicated antibodies (**E**). The fold change in immunoprecipitated NSP4-FLAG was calculated by normalization to immunoprecipitated GFP-NSP3. N = 3 (**F**). All data are presented as mean ± SEM, using unpaired two-tailed *t*-test, ns, no significance.

the T492I mutation influences this homodimerization. Co-expressing NSP4 (WT)-FLAG and GFP-NSP4 (WT) or NSP4 (T492I)-FLAG and GFP-NSP4 (T492I), co-IP results revealed that GFP-NSP4 was co-precipitated by NSP4-FLAG (Fig. 4A), consistent with earlier observations (Hagemeijer et al., 2011). However, the ratio of GFP-NSP4 to NSP4-FLAG in the precipitation for the T492I mutation was notably higher than that for the WT (Fig. 4A and B), suggesting that the NSP4 T492I mutation enhances its homodimerization. Furthermore, a bimolecular fluorescence complementation (BiFC) assay was employed as a complementary method to assess homodimerization (Kerppola, 2006). This technique utilizes two split YFP reporter fragments, nYFP, and cYFP, fused to the proteins of interest. Upon interaction between the fusion proteins, YFP fluorescent reporter activity is reconstituted. C-terminal nYFP and cYFP reporter fusion constructs of NSP4 (WT or T492I) were generated and co-expressed in HEK293T cells, after which the cells were processed for quantitative fluorescence analysis. The results demonstrated a higher number of YFP-positive cells when co-expressing NSP4 (T492I)-nYFP and NSP4 (T492I)-cYFP compared to NSP4 (WT)-nYFP and NSP4 (WT)-cYFP (Fig. 4C and D), providing additional evidence of increased homodimerization induced by the NSP4 T492I mutation.

We went on to explore whether the increased homodimerization of NSP4 could lead to changes in the size of puncta induced by co-expression of NSP3/4. Co-expressing GFP-NSP3 with either NSP4 (WT)-mCherry or NSP4 (T492I)-mCherry in HeLa cells revealed that the GFP and mCherry fluorescent signals co-localized in puncta structures (Fig. 4E), consistent with previous findings (Ji et al., 2022). The number and distribution of fluorescent puncta per cell induced by NSP3 with NSP4 (WT) or NSP4 (T492I) remained unchanged (Fig. 4F). However, the average size of fluorescent puncta induced by NSP4 (T492I) with NSP3 was significantly larger compared to those induced by NSP4 (WT) with NSP3 (Fig. 4F). Additionally, the percentage of larger fluorescent puncta induced by NSP4 (T492I) with NSP3 was higher than those induced by NSP4 (WT) with NSP3 (Fig. 4F). These results suggest that the NSP4 T492I mutation, which enhances homodimerization, can lead to an increase in the size of puncta formed in collaboration with NSP3.

NSP4 T492I mutation increases ER membrane curvature and the DMV density per fluorescent puncta

The homodimerization is necessary for ER morphogenic proteins to regulate ER curvature (Wang et al., 2021), which promotes us to investigate the potential impact of the NSP4 T492I mutation on increasing ER curvature. By investigating the curvature of the ER membrane, with a smaller radius indicating higher curvature, we aimed to understand the role of NSP4 T492I mutation in regulating this aspect. Through experiments involving the co-expression of NSP3/NSP4 (WT or T492I)/NSP6 in HEK293T cells, it was observed that the T492I mutant samples exhibited a higher prevalence of ER segments with smaller radii of curvature compared to the WT samples (Fig. 5A and B and Supplementary Fig. S2). Specifically, the peak radius of curvature was notably reduced in the T492I mutant samples (Fig. 5B), indicating a higher degree of membrane curvature facilitated by the mutation in the presence of NSP3 and NSP6.

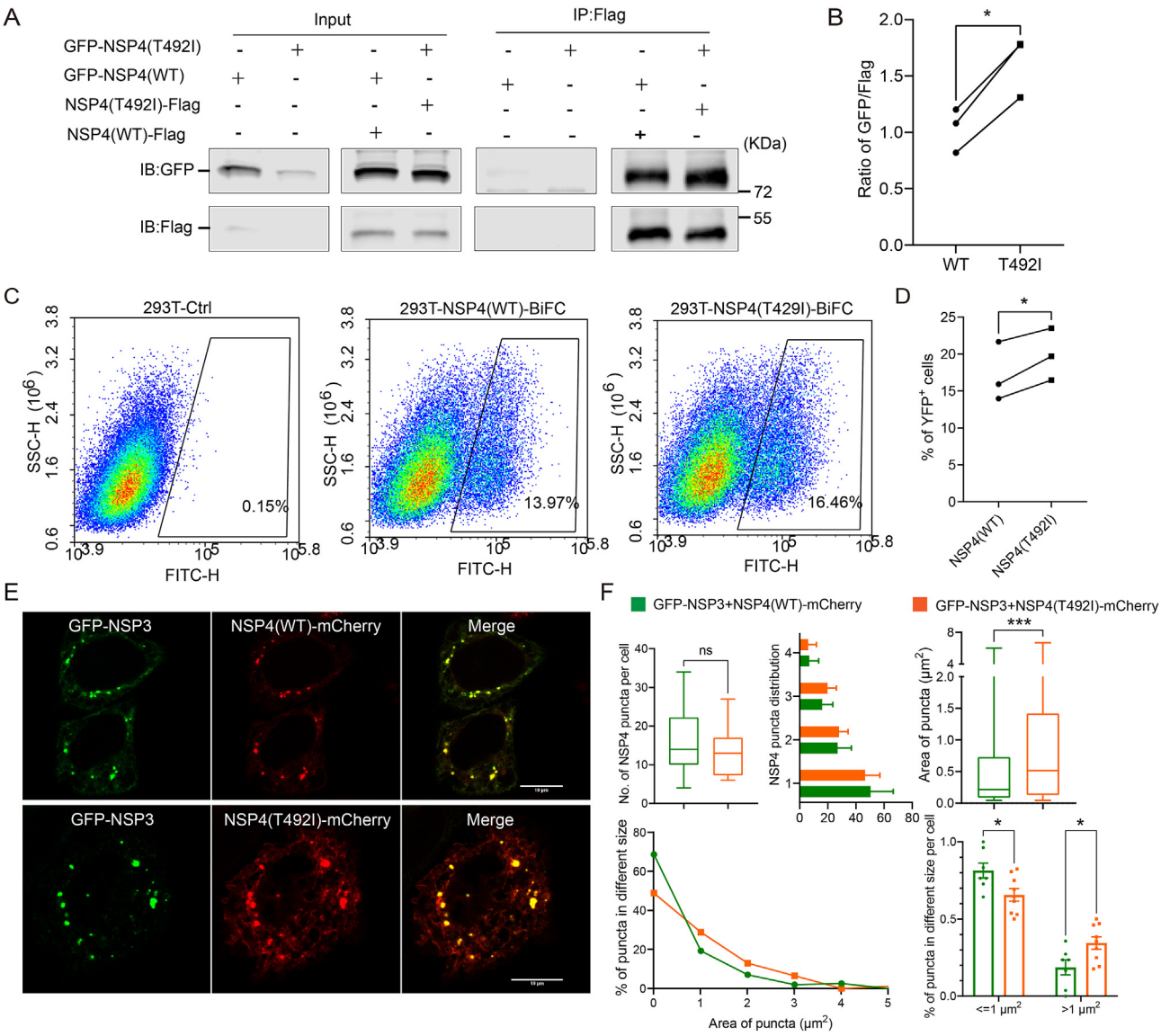

Fig. 4. NSP4 T492I mutation increases its homodimerization and the size of puncta induced by NSP3/4. **A** Co-IP analysis of the effect of T492I mutation on the homodimerization of NSP4. HEK293T cells co-expressing GFP-NSP4 (WT) and NSP4-FLAG (WT), or GFP-NSP4 (T492I) and NSP4-FLAG (T492I) were lysed, and immunoprecipitates pulled down by FLAG antibody were analyzed by immunoblotting with the indicated antibodies. **B** The fold change in immunoprecipitated GFP-NSP4 was calculated by normalization to immunoprecipitated NSP4-FLAG. N = 3. All data are shown in mean ± SEM, using paired two-tailed *t*-test, $^*P < 0.05$, significant. **C** BiFC analysis of the effect of T492I mutation on the homodimerization of NSP4. HEK293T cells transfected with NSP4-nYFP (WT) + NSP4-cYFP (WT) or NSP4-nYFP (T492I) + NSP4-cYFP (T492I) were analyzed by flow cytometry. Non-transfected HEK293T cells served as a negative control. **D** Quantitative analysis of the YFP-positive rate. N = 3 (**D**). All data are shown in mean ± SEM, using paired two-tailed *t*-test, $^*P < 0.05$, significant. **E** Representative confocal images of the puncta structure induced by GFP-NSP3 and NSP4-mCherry in HeLa cells. **F** Quantitative analysis of the number (upper panel, left), distribution (upper panel, middle) and size (upper panel, right and lower panel) of puncta structure induced by NSP3 and NSP4 (WT and T492I). The puncta were divided into quadrants to characterize the distribution. Histogram of puncta area shows that NSP4 (T492I) is more likely to form larger puncta with NSP3. Specifically, fluorescent puncta larger than 1um occur with a higher probability in NSP4 (T492I) cells compared to NSP4 (WT) cells. Box plots represent 25th to 75th percentiles of the data (centre line, median; whiskers, minima and maxima). All data are shown in Mean ± SEM, N = 3, n = 8. Unpaired two-tailed *t*-test, $^*P < 0.05$ and $^{***}P < 0.001$.

Further validation was carried out by assessing ER membrane curvature in samples expressing only NSP4. By generating HEK293T cells that stably expressed NSP4 (WT or T492I)-mCherry, the results showed that even in the context of expressing only NSP4, the T492I mutation led to an alteration in ER curvature (Fig. 5C and D), resulting in a more curved ER membrane. These findings suggest that the NSP4 T492I mutation plays a significant role in modulating ER membrane curvature.

To further confirm whether the increased ER membrane curvature induced by the NSP4 T492I mutation leads to the formation of more DMVs, we performed cryo-correlated light and electron microscopy (cryo-CLEM) in HeLa cells co-expressing GFP-NSP3 with either NSP4 (WT)-mCherry or NSP4 (T492I)-mCherry. To increase the targeting efficiency, the lamellae was prepared by a cryogenic correlated light, ion and electron microscopy (cryo-CLIEM) technique under the guidance of three-dimensional confocal imaging, which was developed by our colleagues (Supplementary Fig. S3) (Li et al., 2023). Cryo-ET results showed that the NSP3/4$^+$ puncta consisted of multiple DMVs with an average diameter of 100 nm (Fig. 5E–H, **Videos S1** and **S2**), consistent with previous studies (Zimmermann et al., 2023). 3D segmentations illustrated that these DMVs were frequently linked to ER membranes (Fig. 5E–H), suggesting their origin from the ER. Quantitative analysis revealed that fluorescent puncta induced by NSP4 (T492I) with NSP3 contained more DMVs compared to those induced by NSP4 (WT) with NSP3 (Fig. 5F1 and 5H1). Through the exceptional imaging capabilities

of cryo-EM, we could observe the pore complexes on the DMVs (Fig. 5I). Investigation into the effect of the T492I mutation on these pore complexes demonstrated no significant changes between the WT and T492I-mutated NSP4 (Fig. 5J and K). Furthermore, quantitative analysis of the DMV density was performed using conventional EM, where the total numbers of DMVs within approximately 0.5 or 1 μm of each DMV were measured. The findings indicated that for both the 0.5 and 1 μm per DMV analyses, the number of DMVs in cells expressing the NSP4 (T492I)

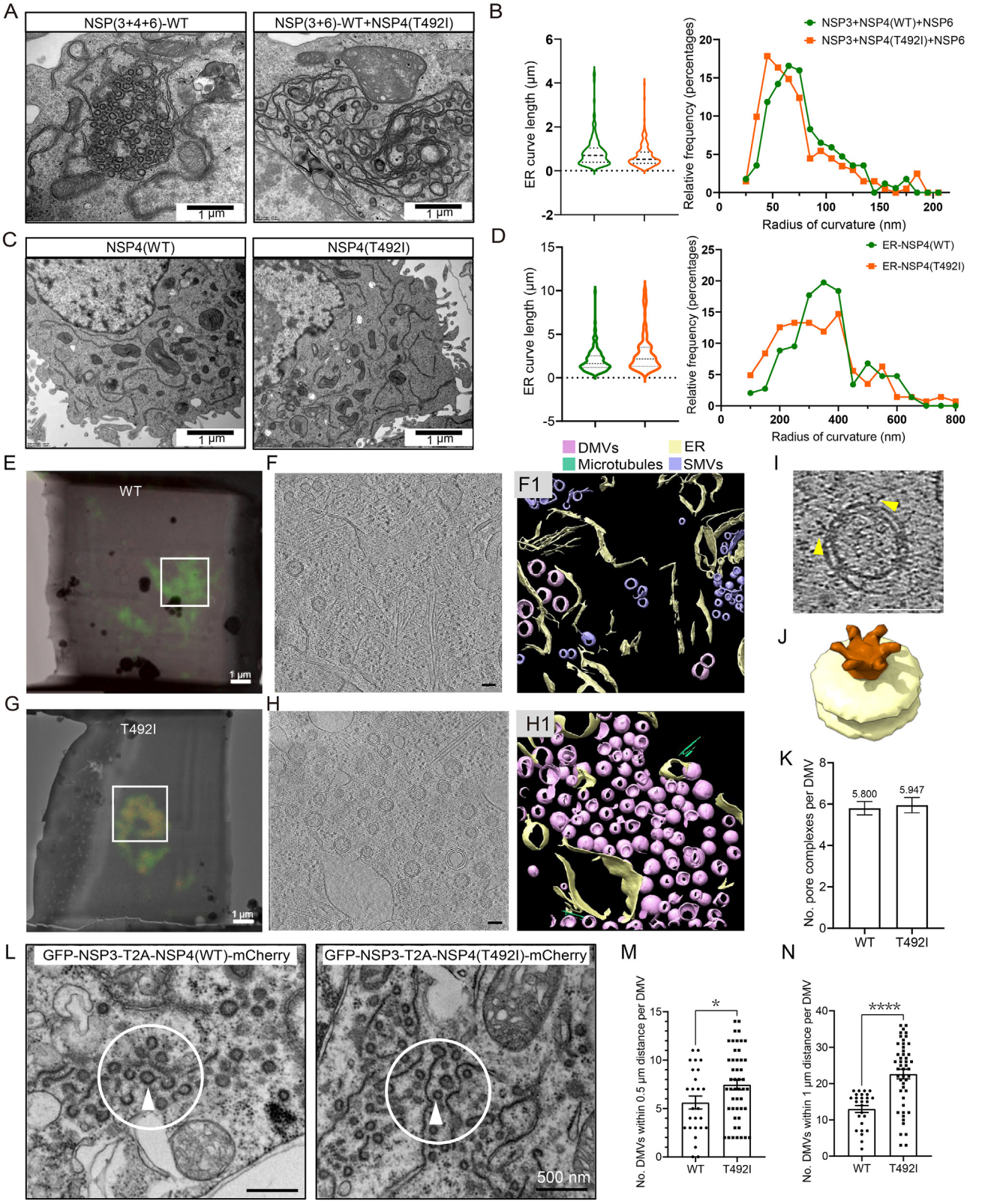

(caption on next page)

was higher than in those expressing the NSP4 (WT) (Fig. 5L–N). These results provide strong evidence that the DMV density is increased in cells harboring the NSP4 (T492I) compared to those with the NSP4 (WT).

Supplementary video related to this article can be found at https://doi.org/10.1016/j.virs.2025.03.010

DISCUSSION

In this study, we conducted a systematic analysis of the impact of NSP3/4/6 Omicron BA.1 mutations on DMV formation and their evolution in SARS-CoV-2 variants. We observed that the NSP4 T492I mutation, present from the Delta variant to Omicron sub-lineages, significantly enhances DMV formation. However, NSP3 mutations exclusive to Omicron BA.1, with the exception of the A1892T mutation also found in Omicron JN.1 sub-lineage, do not influence DMV formation. Regarding NSP6 mutations, the L105Δ and I189V mutations specific to Omicron BA.1, while the SG106/107Δ mutations are prevalent in Alpha, Beta, Gamma, and all Omicron sub-lineages of SARS-CoV-2 but absent in the Delta variant. Combined, these mutations have no effect on DMV formation. An additional study notes that the SGF106/107/108Δ mutations, emerging independently in the Alpha, Beta, Gamma and Lambda variants of SARS-CoV-2, function as gain-of-function mutants with increased ER-zippering activity, promoting DMV formation (Ricciardi et al., 2022). Further examination of mutations in Omicron sub-lineages reveals the presence of the NSP6 SGF106/107/108Δ mutation in all subsequent Omicron sub-lineages. These findings underscore the importance of increased DMV formation as a key mechanism for promoting SARS-CoV-2 transmission.

In our investigation, we identified that the NSP4 T492I mutation enhances its homodimerization, resulting in enlarged puncta induced by NSP3/4 and increased ER membrane curvature, thereby boosting DMV density per fluorescent puncta. A recent study, conducted during the preparation of our manuscript, suggests that the NSP4 T492I mutation enhances SARS-CoV-2 transmissibility and adaptability by improving the cleavage efficiency of the viral main protease NSP5 (Lin et al., 2023). We introduce an additional mechanism in our study to elucidate how the NSP4 T492I mutation enhances SARS-CoV-2 transmissibility and adaptability through promoting DMV formation. The combined action of these two mechanisms synergistically enhances the transmission of the SARS-CoV-2 Omicron variant.

In addition to the insights provided by this study, the research suggests that NSP4 serves as an ER morphogenic protein. The NSP4 T492I mutation enhances its homodimerization and curvature of the ER membrane. Previous studies have demonstrated that the formation of homodimers is a critical mechanism for ER morphogenic proteins such as REEP and reticulon in inducing high ER membrane curvature (Wang et al., 2021). Furthermore, the presence of an amphipathic helix domain is vital for ER morphogenic proteins to generate curvature. For example, the amphipathic helix domain in NSP6 plays a crucial role in the formation of zippered ER structures (Ricciardi et al., 2022). Therefore, it would be of interest to investigate the potential role of NSP4 in assembling tubular ER structures *in vitro*, given its potential contribution to ER morphogenesis.

CONCLUSIONS

In conclusion, the NSP4 T492I mutation in SARS-CoV-2, prevalent across Delta and Omicron sub-lineages, enhances DMV formation through two distinct mechanisms: promoting NSP4 homodimerization and increasing ER membrane curvature. Systematic analyses using TEM, cryo-CLEM, and biochemical assays revealed that the mutation amplifies DMV density per puncta, facilitating viral replication. In contrast, NSP3 and NSP6 mutations showed negligible impact. Genomic sequencing confirmed the T492I mutation correlates with heightened viral transmissibility. These findings underscore the critical role of NSP4 in SARS-CoV-2 evolution, providing insights into how ER morphogenic protein modifications influence viral pathogenesis and adaptability.

MATERIALS AND METHODS

Antibodies

Primary antibodies: rabbit monoclonal anti-GFP (Proteintech, 50430-2-AP), mouse anti-Flag (Proteintech, 66008-4-Ig), rabbit anti-GAPDH (Bioworld, AP0063), mouse anti-mCherry (Ray Antibody, RM1011). HRP-conjugated secondary antibodies: goat anti-rabbit IgG (H + L) (Ray Antibody, RM3002), goat anti-mouse IgG (H + L) (Ray Antibody, RM3001).

Fluorescence-labelled secondary antibodies: IRDye 680 goat anti-rabbit (LI-COR Biosclences, 926–68070) and IRDye 800 goat anti-mouse (LI-COR Biosclences, 926–32211).

Plasmid constructs

GFP-NSP3 (pEGFP-C1 vector), NSP4-mCherry (pLVX-EF1a-IRES-Puro vector) plasmids were kindly provided by Prof. Hong Zhang (Institute of Biophysics, Chinese Academy of Sciences, Beijing, China). GFP-NSP4 was generated by replacing the NSP3 fragment of GFP-NSP3 with NSP4. NSP4-FLAG, NSP-BFP were generated by replacing the mCherry fragment of NSP4-mCherry with FLAG and BFP, respectively. NSP4-nYFP and NSP4-cYFP were generated by replacing nYFP (1–154) or cYFP (155–238) with mCherry fragment of NSP4-mCherry.

NSP6 was amplified by PCR using SARS-CoV-2 replicon (a gift from Prof. Hui Zhang, Zhongshan School of Medicine, Sun Yat-sen University). NSP6-iRFP was generated by inserting NSP6 and iRFP fragments into pLVX-EF1a-IRES-Puro vector. The mCherry-NSP6 was generated by inserting mCherry and NSP6 fragments into pLVX-EF1a-IRES-Puro vector.

GFP-NSP3 (K38R, S1265Δ, L1266I, A1892T) (referred to as NSP3(Omi) in the text), NSP4(T492I)-mCherry, NSP6(LSG105, 106,107Δ, I189V)-iRFP (referred to as NSP6(Omi) in the text), NSP4(T492I)-FLAG, GFP-NSP4(T492I), NSP4(T492I)-nYFP and NSP4(T492I)-cYFP were generated by PCR-based mutagenesis from GFP-nsp3, NSP4-mCherry, NSP6-iRFP, NSP4-FLAG, GFP-NSP4, NSP4-nYFP and NSP4-cYFP, respectively. mCherry-NSP6(Omi) was modified from NSP6(Omi)-iRFP by replace the iRFP tag.

Fig. 5. NSP4 T492I mutation increases ER membrane curvature and the DMV density per fluorescent puncta. **A** TEM images of ER containing DMV regions in NSP3/4/6 samples. **B** Statistical graph of the total ER membrane length and distribution curve of ER membrane curvature for NSP3/4/6 WT and T492I mutation samples. **C** TEM images of ER in HEK293T cells only expressing WT or T492I mutant NSP4. **D** Statistical graph of the total ER membrane length and distribution curve of ER membrane curvature for NSP4 WT and T492I mutation samples. **E–H** Cryo-CLEM image of HeLa cells co-expressing GFP-NSP3 and NSP4 (WT or T492I)-mCherry. White box indicates the area for cryo-ET data collection (WT for **E, F** and **F1**; T492I for **G, H** and **H1**). Averaged tomographic slice and segmentation of the area depicted in figure E, showing a small number of DMVs induce by NSP3 and NSP4 (WT) (**F** and **F1**). Averaged tomographic slice and segmentation of the area depicted in figure G, showing a large number of DMVs induced by NSP3 and NSP4 (T492I) (**H** and **H1**). Pink represents DMV, yellow represents ER, purple represents single membrane vesicle (SMV), and green represents microtubules. **I, J** Averaged slices of a tomogram showing a single DMV with multiple pores spanning two membranes. Yellow arrows indicate the pores. Isosurface representation of the filtered C6 symmetrized subtomogram average of SARS-CoV-2 GFP-NSP3 and NSP4-mCherry showing the pore complex with its crown on the convex side of the double membrane. **K** Quantitative analysis of the number of transmembrane pore complexes per DMV induced by WT or T492I mutant NSP4 with NSP3. N = 3, n = 20, mean ± SEM, unpaired two-tailed *t*-test. **L** Conventional TEM image of DMVs cluster induced by GFP-NSP3 and NSP4-mCherry (WT and T492I). Arrows and dashed circles indicate the number of DMVs within a certain range around a single DMV. **M–N** The average number of DMVs within 0.5 μm (**M**) and 1 μm (**N**) around each DMV. Mean ± SEM, unpaired two-tailed *t*-test, $^{*}P < 0.05$ and $^{****}P < 0.0001$.

Human C4orf3, METT125B sequence were amplified with HEK293T cell cDNA and subcloned into pmCherry-N1 vector. The full-length sequences of human SMIM12, SLC39A9, KIAA0319L were brought from Sino Biological (China, Beijing) and subcloned into pmCherry-N1 vector.

All plasmids were constructed using NEBuilder® HiFi DNA Assembly Master Mix to insert and replace fragments into plasmid vectors.

Cell culture, transfection and stable cell lines

HeLa and HEK293T cells (from ATCC) were cultured in Dulbecco's modified Eagle's medium (DMEM) medium supplemented with 10% fetal bovine serum (FBS), 100 U/mL Penicillin-Streptomycin (P/S), at 37 °C in a 5% CO_2 incubator. Transfection were performed using the Lipofectamine 3000 Transfection Reagent (Invitrogen).

HeLa cells stably expressing NSP6(WT)-iRFP, NSP6(Omicron)-iRFP, NSP4(WT)-mCherry or NSP4(T492I)-mCherry were prepared as follows. HEK293T cells were transfected with lentivirus plasmid and packaging plasmids psPAX2 and VSVG at the ratio of 4:3:1 with Lipofectamine 3000. After 48 h, the supernatant was collected, filtered with 0.45 μm filter, and then infected with HeLa cells for 48 h. Positive cells were selected using DMEM medium containing puromycin (2 μg/mL). In general, after about two weeks of puromycin selection and verification by fluorescence imaging, HeLa cell lines stably expressing specific proteins can be obtained.

CHX chase assay

HEK293T cells were seeded into 6-well plate at 4×10^5 density and transfected with the indicated plasmids. After 24 h transfection, cells were treated with 100 μg/mL CHX (Meilunbio, MB2208) and collected at different time point for immunoblotting analysis later.

Co-immunoprecipitation (co-IP) and immunoblotting (IB)

For co-IP analysis, cells were transfected with indicated plasmids and harvested after 24–48 h. Cells were washed with PBS and lysed in lysis-buffer (50 mmol/L Tris-HCl pH 7.4, 5 mmol/L EDTA, 40 mmol/L β-sodium glycerophosphate, 30 mmol/L NaF, 1 mmol/L PMSF, 1 mmol/L Na_3VO_4, 10% glycerol, 1% NP-40, and 150 mmol/L NaCl) supplemented with protease inhibitor cocktails (Roche) on ice for 30 min. Centrifuge at 12,000×*g* for 15 min at 4 °C, collect the supernatant and incubate with Anti-DYKDDDDK (FLAG) Magarose Beads (Smart-Lifescience, SM009001) or Anti-GFP Magarose Beads (Smart-Lifescience, SM038001) overnight at 4 °C. The binding proteins were eluted with SDS-PAGE loading buffer and analyzed with IB.

For IB, cells were washed with PBS and then lysed on ice for 30 min in RIPA with 1% protease inhibitor cocktails (Roche). The lysates were centrifuge at 12,000 ×*g*, 4 °C for 15 min and collected the supernatants for SDS-PAGE. The separated proteins were transferred onto NC membrane (Millipore). The membrane was blocked with 5% (w/v) skim milk (BD, 232100) in TBST buffer for 1 h, incubated with primary antibodies overnight at 4 °C and then with HRP-conjugated secondary antibodies (or fluorescence dye-conjugated secondary antibodies) at room temperature for 1 h. The signals were visualized and captured by Tanon 5200 Chemiluminescent Imaging System (Tanon) or Odyssey M system (LI-COR Biosciences).

Confocal microscopy

The cells were imaged by confocal laser scanning microscopy (Olympus FV3000 and Nikon AX). The fluorescent images presented are representative images from at least three independent experiments. Images for phenotypic quantification were obtained with the same parameters (digital gain, laser power, and magnification) and processed with Fiji [ImageJ; National Institutes of Health (NIH)] software.

Number, size and distribution of NSP3/NSP4 puncta

In ImageJ, apply different threshold to segment NSP3/NSP4 fluorescent puncta, and use “Analyze particle” function to measure the number of puncta per cell. For calculation of puncta size, set “Area” as measurement and use “Analyze particle” function.

To calculate the distribution of NSP4 fluorescent puncta in the cell, use the “Analyze particle” function in ImageJ to measure the centroid coordinates of each fluorescent puncta. Get the X and Y coordinates of each punctum. The center of mass of the whole cell was taken as the origin of the coordinate axis, and the XY coordinates of the fluorescent puncta were divided into four quadrants. Calculate the percentage of fluorescent puncta in each quadrant to the total fluorescent puncta.

BiFC assay

HEK293T cells were transfected with -nYFP and -cYFP tagged proteins. After 24 h, the cells were treated at 30 °C for 6 h to allow the fluorophore to mature. Fluorescence positive cells were detected by flow cytometry (Agilent Novocyte Advanteon).

Proteomic analysis

Sample preparation

HEK293T cell were transfected with indicated plasmids and harvested for co-IP sample processing. The co-IP magnetic beads were washed with PBS three times, then digested with trypsin in 100 mmol/L ammonium hydrogen carbonate at 25 °C for 2 h. After reduction/alkylation (5 mmol/L dithiothreitol, 30 min/10 mmol/L Iodoacetamide, 30 min in dark), a second trypsin digestion was performed at 25 °C for 1 h. The reaction was stopped with trifluoroacetic acid, and peptides were purified using C18 StageTips.

LC-MS/MS analysis

Peptides were separated on a nanoElute UHPLC (Bruker Daltonics, Germany) using an Ionopticks Aurora C18 column (250 mm × 75 μm, 1.6 μm) (Ionopticks, Australia). Solvent A was 0.1% formic acid in water, and solvent B was 0.1% formic acid in acetonitrile. The column was maintained at 50 °C. The LC-MS/MS run time was 60 min with the following gradient: 0–45 min: 2%–22% B; 45–50 min: 22%–37% B; 50–55 min: 37%–80% B; 55–60 min: 80% B at 300 nL/min.

The LC was coupled online to a hybrid timsTOF Pro (Bruker Daltonics, Germany) via a CaptiveSpray nano-electrospray ion source. The timsTOF Pro mass spectrometer (Bruker Daltonics, Germany) was run in positive mode with enabled trapped ion mobility spectrometry (TIMS) at 100% duty cycle (100 ms ramp time). Source capillary voltage was 1500 V, and dry gas flow was 3 L/min at 180 °C. Data were acquired in data independent parallel accumulation–serial fragmentation (diaPASEF), covering an *m/z* range from 350 to 1550, a mobility range of 0.75–1.3 Vs/cm2 (1/K0) and 14 dia-PASEF scans. Collision energy increased linearly from 20 to 59 eV over the mobility range (for 1/K0 values between 0.6 and 1.6, 20–59 eV correspondingly). The total DIA cycle time was 1.59 s.

Data processing

Raw data were analyzed with Spectronaut v18 using “Direct-DIA” for protein identification and quantification. Data were searched against the UniProt human proteome database (20,397 entries, downloaded on October 16, 2022). Trypsin was set as the enzyme with up to two missed cleavages. Carbamidomethylation of cysteine was a static modification;

oxidation of methionine and N-terminal acetylation were dynamic. Other parameters were left at default settings.

Conventional TEM

Cells were harvested and fixed with 2.5% glutaraldehyde in PBS overnight at 4 °C. After 2 × washes with PBS and 2 × washes with ddH_2O, the cells were postfixed in 1% OsO_4 and 1.5% $K_3Fe(CN)_6$ for 1.5 h and then washed with ddH_2O for three times. Cells were dehydrated by a graded series of ethanol solution (30%, 50%, 70%, 80%, 90% and 100%) and embedded in epoxy EMbed 812 resin. The samples were embedded in epoxy EMbed 812 resin and solidified at 45 °C for 12 h and 60 °C for 48 h. Sectioning was performed with a Leica EM UC6 ultramicrotome. The sections were stained with 2% uranyl acetate for 15 min and 1% lead citrate for 5 min. Images were acquired on a 120 kV transmission electron microscope (FEI, Tecnai Spirit) with a CCD camera.

Measurements of DMVs diameters

We use the straight line tool in ImageJ to measure the maximum diameter of each DMV for statistical analysis.

Measurements of ER membrane curvature

We measure the curvature of ER membrane around the DMV cluster (with 1 μm range) by using the "Kappa-curvature analysis" plugin in ImageJ.

DMV density analysis

In EM micrographs, the DMV contour was drown using "freehand selection" in ImageJ. Set the "Center of mass" as measurement parameter and get the centroid coordinates (X, Y) of each DMV. Calculate the distance between every two DMVs. Count the number of other DMVS in the 0.5 μm and 1 μm range for each DMV.

Cryo-CLIEM

Quantifoil R2/1 gold EM grids were plasma cleaned with H_2/O_2 for 30 s in a glow discharge device (Gatan, Plasma Cleaner) and sterilized with UV for 20 min in a biosafety cabinet. HeLa cells were seeded on EM grids in a 35 mm dish at a density of 1×10^5 cells per dish and incubated at 37 °C overnight. Cells were transfected with GFP-NSP3 and NSP4(WT or T492I)-mCherry plasmids. About 24 h after transfection, cells were plunge-frozen in liquid nitrogen by using EM GP2 Automatic Plunge Freezer (Leica). Grids were blotted from back side with 6 s blotting, chamber conditions of 25 °C and 85% humidity, and stored in liquid nitrogen.

Vitrified cells were transferred to a cryo-correlated light, ion and EM (cryo-CLIEM) system that integrates a 3D multicolor confocal microscope into a dual-beam focused ion beam scanning electron microscope (FIB-SEM) (Li et al., 2023). Before FIB milling, 3D LM imaging was performed using an integrated confocal microscope and custom-made software. Tilt the images to same direction as the FIB milling, and determine the milling area according to the fluorescent signal. 500 pA currents were used for rough milling and lower current 50 pA for the polishing step to get the final lamella at 150 nm thickness.

Cryo-electron tomography and sub-tomogram averaging

The lamellae were imaged on a 300 kV Titan Krios electron microscope (Thermo Fisher Scientific) equipped with a field emission gun, a direct electron detector (Gatan, K2 camera) and an energy filter (Gatan). According to the fluorescence position, tilt-series were collected from −60° to +42° at 3° increments using SerialEM software in counting mode, with total accumulated dose of 100 $e^-/Å^2$, defocus of −6 μm, the energy filter of 20 eV and the final pixel size of 4.29 Å. Dose-fractioned images were aligned by MotionCor2 (Zheng et al., 2017). The corrected tilt-series were aligned with AreTomo (Zheng et al., 2022) and reconstructed by WBP implemented in the IMOD software package (Kremer et al., 1996). The tomograms were segmented with EMAN2 (Chen et al., 2017) and visualized with UCSF Chimera (Pettersen et al., 2004).

The identification and selection of DMV membrane pore complex (MPC) was done manually using Dynamo packages (Castano-Diez et al., 2012). Initial Euler angles for two out of three directions were determined based on the vector from a manually selected point in the MPC transmembrane region to another at the center of the DMV. To avoid any model bias, an average reconstruction of all particles was generated as an initial alignment reference within RELION (Bharat and Scheres, 2016), where C6 symmetry was always enforced. The 3D classification was applied with restrictions on the search range for rotation and tilt angles, choose highest quality particles to do the auto-refinement.

Statistical analysis

Statistical analyses were performed using GraphPad Prism9 (GraphPad Software). All experiments with statistical data were performed three times; N represents the number of experiments, and n represents the total number of measurements or observations. Test data of normal distribution and homogeneity of variance between groups. When the data were normally distributed, *t*-test or ANOVA analysis was used to determine the differences between groups. Nonparametric Mann-Whitney or Kruskal-Wallis tests were performed when the data were not normally distributed.

DATA AVAILABILITY

All the data generated during the current study are included in the manuscript. The videos for 3D reconstruction and segmentation of DMVs in Fig. 5 are available in Science Data Bank with https://doi.org/10.57760/sciencedb.21119.

ETHICS STATEMENT

This article does not contain any studies with human or animal subjects performed by any of the authors.

AUTHOR CONTRIBUTIONS

Pei Wang: formal analysis, investigation, validation, visualization, writing-original draft, writing-review & editing. Buyun Tian: investigation. Ke Xiao: investigation. Wei Ji: funding acquisition, resources. Zonghong Li: conceptualization, funding acquisition, project administration, resources, supervision, writing-original draft, writing-review & editing. All the authors discussed the data and reviewed the manuscript.

CONFLICT OF INTEREST

The authors declare that they have no conflict of interest.

ACKNOWLEDGMENTS

The TEM studies were performed at the Center for Biological Imaging (CBI), Institute of Biophysics, Chinese Academy of Sciences. We thank Xixia Li, Zhongshuang Lv, Xueke Tan and Can Peng at CBI for their assistance in EM sample preparations. We thank Qing Zhang from Proteomics and Metabolomics Core Facility, Guangzhou National Laboratory, for her assistance with the MS sample preparation and analysis. This work was supported by the National Natural Science Foundation of China (92469107 to Z. Li), the R&D Program of Guangzhou National Laboratory (ZL-SRPG2200205 to Z. Li), and the Guangdong Province High-level Talent Youth Project (2021QN02Y939 to Z. Li).

APPENDIX A. SUPPLEMENTARY DATA

Supplementary data to this article can be found online at https://doi.org/10.1016/j.virs.2025.03.010.

REFERENCES

Angelini, M.M., Akhlaghpour, M., Neuman, B.W., Buchmeier, M.J., 2013. Severe acute respiratory syndrome coronavirus nonstructural proteins 3, 4, and 6 induce double-membrane vesicles. mBio 4, e00524-13.

Bharat, T.A., Scheres, S.H., 2016. Resolving macromolecular structures from electron cryo-tomography data using subtomogram averaging in RELION. Nat. Protoc. 11, 2054–2065.

Cao, Y., Yisimayi, A., Jian, F., Song, W., Xiao, T., Wang, L., Du, S., Wang, J., Li, Q., Chen, X., et al., 2022. BA.2.12.1, BA.4 and BA.5 escape antibodies elicited by Omicron infection. Nature 608, 593–602.

Castano-Diez, D., Kudryashev, M., Arheit, M., Stahlberg, H., 2012. Dynamo: a flexible, user-friendly development tool for subtomogram averaging of cryo-EM data in high-performance computing environments. J. Struct. Biol. 178, 139–151.

Chen, D.Y., Chin, C.V., Kenney, D., Tavares, A.H., Khan, N., Conway, H.L., Liu, G., Choudhary, M.C., Gertje, H.P., O'connell, A.K., et al., 2023. Spike and nsp6 are key determinants of SARS-CoV-2 Omicron BA.1 attenuation. Nature 615, 143–150.

Chen, M., Dai, W., Sun, S.Y., Jonasch, D., He, C.Y., Schmid, M.F., Chiu, W., Ludtke, S.J., 2017. Convolutional neural networks for automated annotation of cellular cryo-electron tomograms. Nat. Methods 14, 983–985.

Deng, X., Garcia-Knight, M.A., Khalid, M.M., Servellita, V., Wang, C., Morris, M.K., Sotomayor-Gonzalez, A., Glasner, D.R., Reyes, K.R., Gliwa, A.S., et al., 2021. Transmission, infectivity, and neutralization of a spike L452R SARS-CoV-2 variant. Cell 184, 3426–3437 e3428.

Gu, H., Krishnan, P., Ng, D.Y.M., Chang, L.D.J., Liu, G.Y.Z., Cheng, S.S.M., Hui, M.M.Y., Fan, M.C.Y., Wan, J.H.L., Lau, L.H.K., Cowling, B.J., Peiris, M., Poon, L.L.M., 2022. Probable transmission of SARS-CoV-2 Omicron variant in quarantine hotel, Hong Kong, China, november 2021. Emerg. Infect. Dis. 28, 460–462.

Hagemeijer, M.C., Ulasli, M., Vonk, A.M., Reggiori, F., Rottier, P.J., De Haan, C.A., 2011. Mobility and interactions of coronavirus nonstructural protein 4. J. Virol. 85, 4572–4577.

Harvey, W.T., Carabelli, A.M., Jackson, B., Gupta, R.K., Thomson, E.C., Harrison, E.M., Ludden, C., Reeve, R., Rambaut, A., Consortium, C.-G.U., Peacock, S.J., Robertson, D.L., 2021. SARS-CoV-2 variants, spike mutations and immune escape. Nat. Rev. Microbiol. 19, 409–424.

Hou, Y.J., Chiba, S., Halfmann, P., Ehre, C., Kuroda, M., Dinnon 3rd, K.H., Leist, S.R., Schafer, A., Nakajima, N., Takahashi, K., et al., 2020. SARS-CoV-2 D614G variant exhibits efficient replication ex vivo and transmission in vivo. Science 370, 1464–1468.

Ji, M., Li, M., Sun, L., Zhao, H., Li, Y., Zhou, L., Yang, Z., Zhao, X., Qu, W., Xue, H., Zheng, Z., Li, Y., Deng, H., Zhao, Y.G., 2022. VMP1 and TMEM41B are essential for DMV formation during beta-coronavirus infection. J. Cell Biol. 221, e202112081.

Kehrer, T., Cupic, A., Ye, C., Yildiz, S., Bouhaddou, M., Crossland, N.A., Barrall, E.A., Cohen, P., Tseng, A., Cagatay, T., et al., 2023. Impact of SARS-CoV-2 ORF6 and its variant polymorphisms on host responses and viral pathogenesis. Cell Host Microbe 31, 1668–1684 e1612.

Kerppola, T.K., 2006. Design and implementation of bimolecular fluorescence complementation (BiFC) assays for the visualization of protein interactions in living cells. Nat. Protoc. 1, 1278–1286.

Klein, S., Cortese, M., Winter, S.L., Wachsmuth-Melm, M., Neufeldt, C.J., Cerikan, B., Stanifer, M.L., Boulant, S., Bartenschlager, R., Chlanda, P., 2020. SARS-CoV-2 structure and replication characterized by in situ cryo-electron tomography. Nat. Commun. 11, 5885.

Knoops, K., Kikkert, M., Worm, S.H., Zevenhoven-Dobbe, J.C., Van Der Meer, Y., Koster, A.J., Mommaas, A.M., Snijder, E.J., 2008. SARS-coronavirus replication is supported by a reticulovesicular network of modified endoplasmic reticulum. PLoS Biol. 6, e226.

Kremer, J.R., Mastronarde, D.N., Mcintosh, J.R., 1996. Computer visualization of three-dimensional image data using IMOD. J. Struct. Biol. 116, 71–76.

Li, W., Lu, J., Xiao, K., Zhou, M., Li, Y., Zhang, X., Li, Z., Gu, L., Xu, X., Guo, Q., Xu, T., Ji, W., 2023. Integrated multimodality microscope for accurate and efficient target-guided cryo-lamellae preparation. Nat. Methods 20, 268–275.

Lin, X., Sha, Z., Trimpert, J., Kunec, D., Jiang, C., Xiong, Y., Xu, B., Zhu, Z., Xue, W., Wu, H., 2023. The NSP4 T492I mutation increases SARS-CoV-2 infectivity by altering non-structural protein cleavage. Cell Host Microbe 31, 1170–1184 e1177.

Pettersen, E.F., Goddard, T.D., Huang, C.C., Couch, G.S., Greenblatt, D.M., Meng, E.C., Ferrin, T.E., 2004. UCSF chimera - a visualization system for exploratory research and analysis. J. Comput. Chem. 25, 1605–1612.

Ricciardi, S., Guarino, A.M., Giaquinto, L., Polishchuk, E.V., Santoro, M., Di Tullio, G., Wilson, C., Panariello, F., Soares, V.C., Dias, S.S.G., Santos, J.C., Souza, T.M.L., Fusco, G., Viscardi, M., Brandi, S., Bozza, P.T., Polishchuk, R.S., Venditti, R., De Matteis, M.A., 2022. The role of NSP6 in the biogenesis of the SARS-CoV-2 replication organelle. Nature 606, 761–768.

Souza, P.F.N., Mesquita, F.P., Amaral, J.L., Landim, P.G.C., Lima, K.R.P., Costa, M.B., Farias, I.R., Belem, M.O., Pinto, Y.O., Moreira, H.H.T., Magalhaes, I.C.L., Castelo-Branco, D., Montenegro, R.C., De Andrade, C.R., 2022. The spike glycoprotein of SARS-CoV-2: a review of how mutations of spike glycoproteins have driven the emergence of variants with high transmissibility and immune escape. Int. J. Biol. Macromol. 208, 105–125.

Tabata, K., Prasad, V., Paul, D., Lee, J.Y., Pham, M.T., Twu, W.I., Neufeldt, C.J., Cortese, M., Cerikan, B., Stahl, Y., et al., 2021. Convergent use of phosphatidic acid for hepatitis C virus and SARS-CoV-2 replication organelle formation. Nat. Commun. 12, 7276.

Tchesnokova, V., Kulasekara, H., Larson, L., Bowers, V., Rechkina, E., Kisiela, D., Sledneva, Y., Choudhury, D., Maslova, I., Deng, K., Kutumbaka, K., Geng, H., Fowler, C., Greene, D., Ralston, J., Samadpour, M., Sokurenko, E., 2021. Acquisition of the L452R mutation in the ACE2-binding interface of spike protein triggers recent massive expansion of SARS-CoV-2 variants. J. Clin. Microbiol. 59, e0092121.

Thorne, L.G., Bouhaddou, M., Reuschl, A.K., Zuliani-Alvarez, L., Polacco, B., Pelin, A., Batra, J., Whelan, M.V.X., Hosmillo, M., Fossati, A., et al., 2022. Evolution of enhanced innate immune evasion by SARS-CoV-2. Nature 602, 487–495.

Wang, N., Clark, L.D., Gao, Y., Kozlov, M.M., Shemesh, T., Rapoport, T.A., 2021. Mechanism of membrane-curvature generation by ER-tubule shaping proteins. Nat. Commun. 12, 568.

WHO, 2024. Tracking SARS-CoV-2 variants. https://www.who.int/activities/tracking-SARS-CoV-2-variants/. (Accessed 22 March 2025).

Wolff, G., Limpens, R., Zevenhoven-Dobbe, J.C., Laugks, U., Zheng, S., De Jong, A.W.M., Koning, R.I., Agard, D.A., Grunewald, K., Koster, A.J., Snijder, E.J., Barcena, M., 2020. A molecular pore spans the double membrane of the coronavirus replication organelle. Science 369, 1395–1398.

Wu, H., Xing, N., Meng, K., Fu, B., Xue, W., Dong, P., Tang, W., Xiao, Y., Liu, G., Luo, H., Zhu, W., Lin, X., Meng, G., Zhu, Z., 2021. Nucleocapsid mutations R203K/G204R increase the infectivity, fitness, and virulence of SARS-CoV-2. Cell Host Microbe 29, 1788–1801 e1786.

Xie, X., Liu, Y., Liu, J., Zhang, X., Zou, J., Fontes-Garfias, C.R., Xia, H., Swanson, K.A., Cutler, M., Cooper, D., Menachery, V.D., Weaver, S.C., Dormitzer, P.R., Shi, P.Y., 2021. Neutralization of SARS-CoV-2 spike 69/70 deletion, E484K and N501Y variants by BNT162b2 vaccine-elicited sera. Nat. Med. 27, 620–621.

Yang, J., Tian, B., Wang, P., Chen, R., Xiao, K., Long, X., Zheng, X., Zhu, Y., Sun, F., Shi, Y., Jiu, Y., Ji, W., Xue, Y., Xu, T., Li, Z., 2025. SARS-CoV-2 NSP3/4 control formation of replication organelle and recruitment of RNA polymerase NSP12. JCB (J. Cell Biol.) 224, e202306101.

Yurkovetskiy, L., Wang, X., Pascal, K.E., Tomkins-Tinch, C., Nyalile, T.P., Wang, Y., Baum, A., Diehl, W.E., Dauphin, A., Carbone, C., et al., 2020. Structural and functional analysis of the D614G SARS-CoV-2 spike protein variant. Cell 183, 739–751.e8.

Zheng, S., Wolff, G., Greenan, G., Chen, Z., Faas, F.G.A., Barcena, M., Koster, A.J., Cheng, Y., Agard, D.A., 2022. AreTomo: an integrated software package for automated marker-free, motion-corrected cryo-electron tomographic alignment and reconstruction. J. Struct. Biol. X 6, 100068.

Zheng, S.Q., Palovcak, E., Armache, J.P., Verba, K.A., Cheng, Y., Agard, D.A., 2017. MotionCor2: anisotropic correction of beam-induced motion for improved cryo-electron microscopy. Nat. Methods 14, 331–332.

Zimmermann, L., Zhao, X., Makroczyova, J., Wachsmuth-Melm, M., Prasad, V., Hensel, Z., Bartenschlager, R., Chlanda, P., 2023. SARS-CoV-2 nsp3 and nsp4 are minimal constituents of a pore spanning replication organelle. Nat. Commun. 14, 7894.